High temperature oxidation of additively manufactured Rene 65

M. Huguet[1], G. Boissonnet[1], G. Lotte[1], J. Cormier[2], P. Villechaise[2], G. Bonnet[1], F. Pedraza[1]

martin.huguet@univ-lr.fr, fpedraza@univ-lr.fr

[1] *Université de La Rochelle, Laboratoire des Sciences de l'Ingénieur pour l'Environnement LaSIE UMR-CNRS 7356, Avenue Michel Crépeau, 17042 La Rochelle Cedex 1, France*.

[2] *Institut Pprime, CNRS – ENSMA – Université de Poitiers, UPR CNRS 3346, Department of Physics and Mechanics of Materials, ISAE-ENSMA – Téléport 2, 1 avenue Clément Ader, BP 40109, 86961 Futuroscope Chasseneuil Cedex, France.*

Keywords: Additive manufacturing; Oxidation; High temperature; Superalloy; Rene 65

Abstract: This paper investigates the initial oxidation stages of additive manufactured Rene 65 Ni-based superalloy between 700 and 900 °C in air and argon for 48 h, with different building directions and heat treatments. The results show that the only factor that impact the oxidation behavior is the oxidizing atmosphere. The resulting thin oxide scales are made of $NiCr_2O_4$ and Cr_2O_3 at 700 °C while at 800 and 900 °C the oxide layer is composed of an external Cr_2O_3 layer on top of an internal layer of α-Al_2O_3 due to the lower partial pressure of oxygen underneath the chromia layer.

Highlights:

- AM Rene 65 microstructures do not significantly affect the early stage of oxidation
- At 700, 800 and 900 °C, the oxidation kinetics are similar to those of other turbine disk alloys
- The AM microstructure is sensitive to intergranular oxidation even at low Po_2
- In synthetic air, nitrogen promotes the formation of titanium nitrides under the oxide

1. Introduction

Rene 65 is a nickel-based superalloy developed by General Electric (GE) to be processed using the cast and wrought (C&W) route and with the aim of providing improved capability compared to Inconel 718 (IN718) for aircraft engine components at ever increasing higher operating temperatures [1,2]. IN718 provides a desirable oxidation resistance as well as a high mechanical strength, but its service temperature is limited to approximately 650-670 °C due to the transformation of the strengthening gamma double-prime phase (γ''-(Ni_3Nb)) into the thermodynamically stable but brittle delta phase (δ-(Ni_3Nb)) at higher temperatures [3]. Such embrittlement motivated the engine manufacturers and the supply-chain to develop a new C&W Rene 65 alloy capable to operate at temperatures higher than 650 °C [4]. The chemistry of Rene 65 was optimized from that of Rene 88DT to facilitate C&W processing while reducing the expensive powder metallurgy route of Rene 88DT [1,4].

However, casting and forging of nickel-based superalloys require many fabrication steps, in particular when complex shapes are to be produced. The higher level of design freedom of additive manufacturing (AM) led to the development of additive manufactured parts for the aeronautic industry [5,6]. Static parts made of Rene 65 are currently developed using direct metal laser melting (DMLM) process [7]. In laser melting processes, parameters such as absorbed power, beam velocity or any pre-heating of the substrate can generate thermal cycles during the process that will affect the resulting microstructure [8]. These parameters as well as the building direction have been reported to have an impact on the microstructure and thus on the mechanical properties of the alloy, i.e. DMLM generates microstructures that are highly dependent on the building direction [9]. However, the strength and creep capability of Rene 65 derive from the gamma prime (γ'- $Ni_3(Al, Ti)$) precipitates and from the fine grained microstructure that are both controlled by heat treatment and quenching [1,4,10]. Thus, post-processing treatments such as heat treatment or hot isostatic pressing (HIP) after the DMLM build are needed to obtain the desired microstructure and to reduce or eliminate defects including residual stresses [8]. The influence of the heat treatment (sub-solvus or super-solvus that are respectively, below or above the temperature of γ' solvus) on the final microstructure of Rene 65 was investigated by Wessman et al., who showed that wrought Rene 65 has a fine microstructure in the sub-solvus form because the undissolved γ' precipitates pin the grains boundaries as opposed to the super-solvus counterpart that results in a coarse grain microstructure [4,10].

Since Rene 65 is a γ' strengthened alloy, it is important to evaluate whether the γ' phase is impacted by the heat treatment and the DMLM process. Indeed, it was shown that such precipitates mostly impact the mechanical properties of the superalloys depending on their characteristics (size, volume fraction, morphology) [11]. Moreover, the influence of grain size as well as precipitates size and distribution on the mechanical properties (tensile, low cycle fatigue and creep) of Rene 65 was thoroughly investigated [10,12,13].

Although the microstructural evolution and the mechanical behavior of Rene 65 were studied for long exposure times at high temperature [13], little is known on the reactivity under high temperature oxidizing conditions. Based on the analysis of its mechanical properties and microstructural stability by Wessman et al., Rene 65 can maintain its properties up to 760 °C [10]. Therefore, this study investigates the influence of the microstructure on the oxidation of AM Rene 65 at lower and higher temperatures (700-800-900 °C) and for short times (48 h) allowing to elucidate the role of the building direction (vertical vs. horizontal) and heat treatment (sub-solvus vs. super-solvus), hence the crystal structure, on the early stages of oxidation. Additional annealing tests were performed in Ar to study the metallurgical evolution of Rene 65 at temperatures that can exacerbate the oxidation phenomenon through the few O_2/H_2O ppm contained in the gas flow as demonstrated by Juillet et al. or Bataillou et al. on respectively IN718 and Ni-Cr model alloys [14,15].

2. Material and experimental procedure

Rene 65 was manufactured by the supplier (GE Additive, USA), without specifications on the additive manufacturing parameters as they remain confidential. The rods were manufactured by direct metal laser melting using two building directions (vertical and horizontal, Figure 1) that led to different microstructures at the surface of the coupons. Annealing was performed at super-solvus (1150 °C) or sub-solvus (1050 °C) conditions under hot isostatic pressing, followed by another dwell at the same temperature to reduce internal stresses and a final tempering step at 760 °C. The samples were received after heat treatment with a cylindrical shape (Ø 1.5 cm, 3 cm length) and were cut in 1.5 mm thick coupons. The variety of treatment and building direction led to 4 different coupons. The coupons were first ground with SiC paper down to a grit size of P4000 and then mirror polished with a 1 µm diamond paste prior to any test.

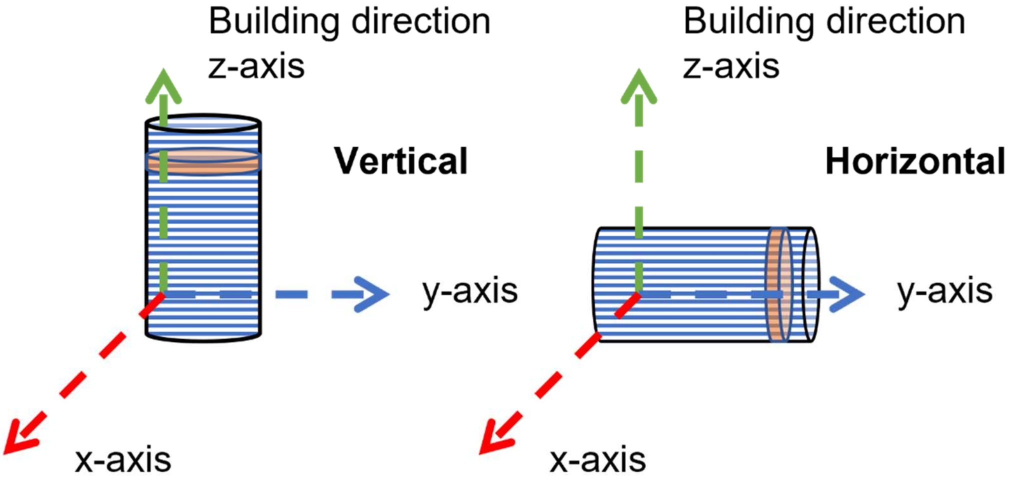

Figure 1: Vertical (a) and horizontal (b) cylindrical samples built along the z axis during additive manufacturing followed by super-solvus or sub-solvus heat treatment both completed with an HIP annealing.

Thermogravimetric analyses (TGA) were performed in a *Setaram Setsys Evolution* apparatus (10^{-7} g accuracy, with 20 mL/min flow rate) in Ar (Air Liquide, *France*, ALPHAGAZ 1, 99.999 % purity, $p_{O2} = 2.10^{-6}$ bar), and dry synthetic air (p_{O2} = 0.2 bar) at 700, 800 and 900 °C for 48 hours. The characterization of as received and oxidized samples was undertaken by optical microscopy (LEICA DMRM) and scanning electron microscopy (SEM, *FEI Quanta 200F,* 20 kV) coupled with an *EDAX* detector for energy dispersive spectroscopy (EDS) allowing to obtain the elemental composition of the analyzed area. The microstructures were revealed by heat tinting the samples in a muffle furnace at 600 °C for 48 hours. The γ' precipitates were revealed by chemical etching using aqua regia (30 mL water, 20 mL hydrochloric acid, and 10 mL nitric acid) to preferentially dissolve the γ' precipitates or by electrochemical attack with oxalic acid at 10 vol.% (2.2 V for 2 to 3 seconds) to dissolve the γ matrix. The various attacks led to images with similar information but different contrasts for image analysis [16]. The size and surface area % of the γ' precipitates were measured from their area by image analysis on 5 images taken in different grains for a total area of about 60 µm². Crystallographic analyses were carried out by electron backscatter diffraction (EBSD) with a *JEOL JSM-6100* scanning electron microscope. The cross sections were obtained using surface abrasion by a focused ion beam of gallium ions in a *Cross beam 340 Zeiss* SEM or by mechanically grinding the samples mounted in a phenolic resin. The samples to be mounted were first protected with a copper electrodeposit (100 mA/cm² for 5 to 10 minutes) to limit the degradation of the oxide scale. The surface finish of the mounted cross-sections was done with Struers-OPS (silica suspension) polishing before electrochemical etching with oxalic acid to reveal the γ' precipitates. The oxide layers were characterized by X-ray diffraction (XRD) using the Cu-Kα radiation (*Bruker AXS D8 Advance*), and by Raman spectrometry (*LabRam HR JOBIN YVON HORIBA* coupled with a *BX51 OLYMPUS* microscope) with a HeNe laser (632.82 nm). The XRD diagrams were taken with an X-ray source kept low and constant at 5° incidence angle to maximize the thin oxide layer response.

3. Results

3.1. As received Rene 65

Table 1 gathers the EDS chemical composition of the four AM Rene 65 averaged from five area (30 µm x 20 µm) analyses. When compared to the nominal composition of the wrought substrate, it appears that AM Rene 65 contains slightly more tungsten at the expense of chromium and nickel, otherwise the proportion of the other elements is practically identical to the composition of the forged alloy within the uncertainty limit of the EDS technique.

Table 1: EDS chemical composition (wt.%) of the four AM Rene 65 compared to the nominal composition of Rene 65 from [4]. Standard error is ± 0.5 wt.%.

Element	Ni	Cr	Co	Ti	Al	Mo	W	Fe	Nb	Zr	B	C
Rene 65	55.5	16.0	13.0	3.7	2.1	4.0	4.0	1.0	0.7	0.05	0.016	0.01
Horizontal super-solvus	52.9	15.3	12.7	3.6	2.3	4.1	6.5	1.5	1.1	-	-	-
Vertical super-solvus	53.6	15.3	12.9	3.6	2.1	3.9	6.2	1.4	1.0	-	-	-
Horizontal sub-solvus	53.4	15.1	12.6	3.7	2.2	4.2	6.2	1.6	1.2	-	-	-
Vertical sub-solvus	53.4	15.3	12.6	3.7	2.2	4.2	6.3	1.3	1.1	-	-	-

Figure 2 shows the microstructure of the different samples in the 3-dimensions (XY, ZY and XZ planes) after a heat tinting treatment on cubic shaped samples. Irrespective of the manufacturing direction, the super-solvus heat treated samples display the same close-to-equiaxed microstructure with an average grain size of 60 ± 20 µm. In contrast, the microstructure of sub-solvus samples is highly dependent on the building direction. The grains are elongated in the direction parallel to the build direction (Z axis) and can reach up to 100 µm in length while they are square-like (equiaxed grains of 40 ± 10 µm) when viewed from a direction perpendicular to the build direction (XY plan).

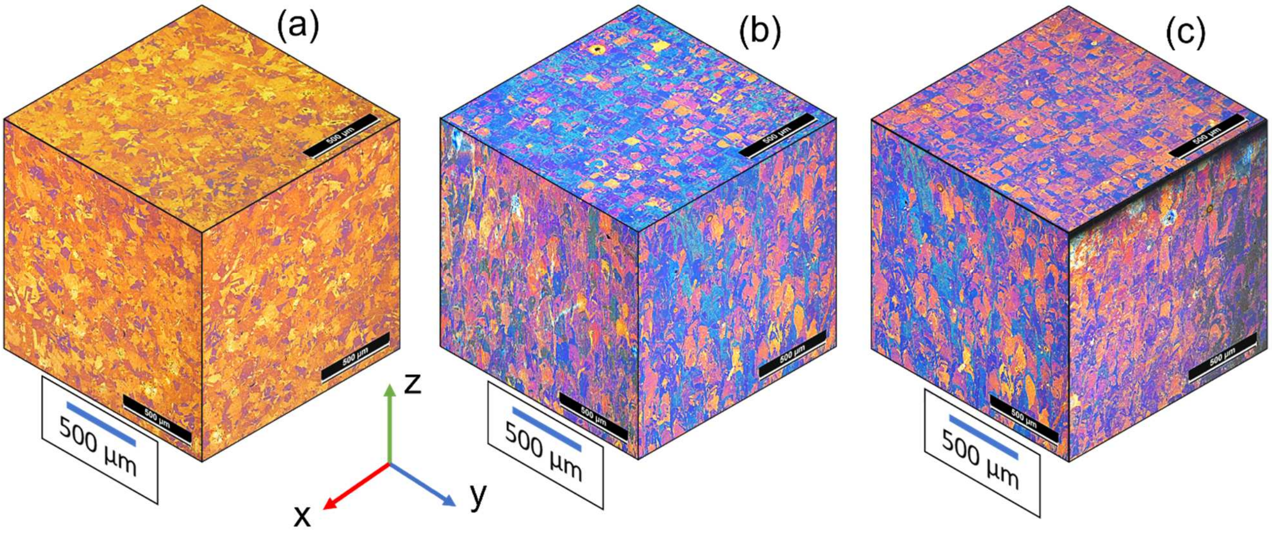

Figure 2: 3D reconstruction of AM Rene 65 microstructure observed from the 3 building plans using optical micrography after heat tinting at 600 °C for 48 hours of (a) Horizontal and Vertical super-solvus, (b) Horizontal sub-solvus, and (c) Vertical sub-solvus samples.

Figure 3 displays EBSD maps for all samples along with corresponding texture index values. When comparing the crystallographic textures of all samples, the two super-solvus samples were found to have similar texture index of 2.5 while sub-solvus samples present a strong [001] texture along the normal direction. The texture index which provides a quantitative measure of the intensity of crystallographic texture along a specific orientation (here the building direction), suggests that sub-solvus samples retain the information of building direction in their structure while the information is erased by the heat treatment for super-solvus samples.

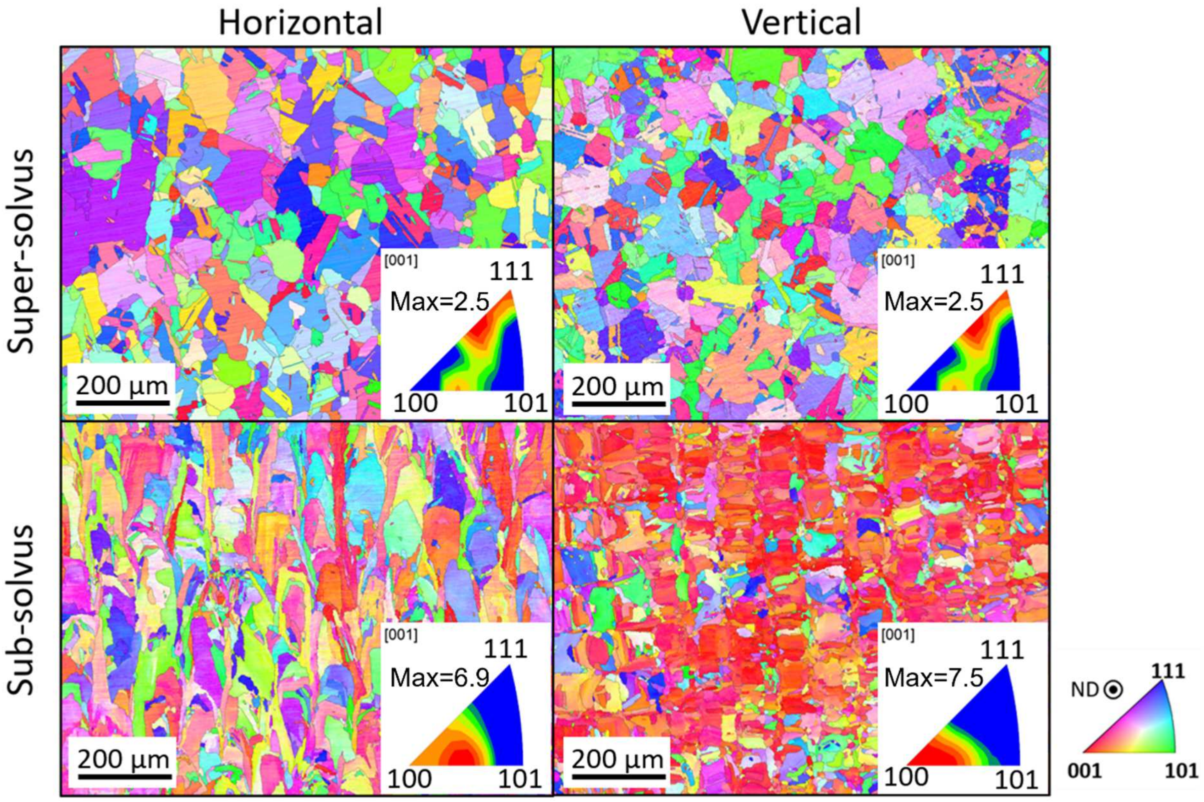

Figure 3: EBSD inverse pole figure coded along normal direction (building direction) of all four samples. Texture maps and maximum texture index are shown in the bottom right-hand corner of each sample.

Figure 4 shows the SEM micrographs of the surfaces of the as-received samples after chemical and electro-chemical etching to reveal the γ/γ' microstructure. At low magnification (Figure 4a), the γ' precipitates appear to be randomly dispersed in the γ-matrix of the super-solvus specimens while they seem to be aligned differently in each grain in the sub-solvus ones. The grain boundaries are highlighted with the dashed lines on the micrographs of Figure 4a. Three populations of precipitates, called primary, secondary and tertiary, can be found in forged Rene 65 depending on their size, the largest being the primary. Only secondary and tertiary γ' precipitates are observed in AM Rene 65 while no primary precipitates were found on the surfaces in good agreement with the work of Wessman et al. [7].

Figure 4b shows the γ' precipitates at higher magnification while Table 2 gathers the results of their average size and surface fraction measured using image analysis from 5 images for each sample. Even if the secondary and tertiary γ' precipitates (large and small size, respectively) vary in shape and size, the overall volume ratio in both sub-solvus and super-solvus specimens is similar. In the super-solvus samples, the secondary precipitates have a rectangular shape while they are more spherical on the sub-solvus samples. Furthermore, the secondary precipitates in the super-solvus samples seem to split into smaller precipitates while the sub-solvus ones maintain their circular shape. In all the samples, the tertiary γ' precipitates are almost spherical.

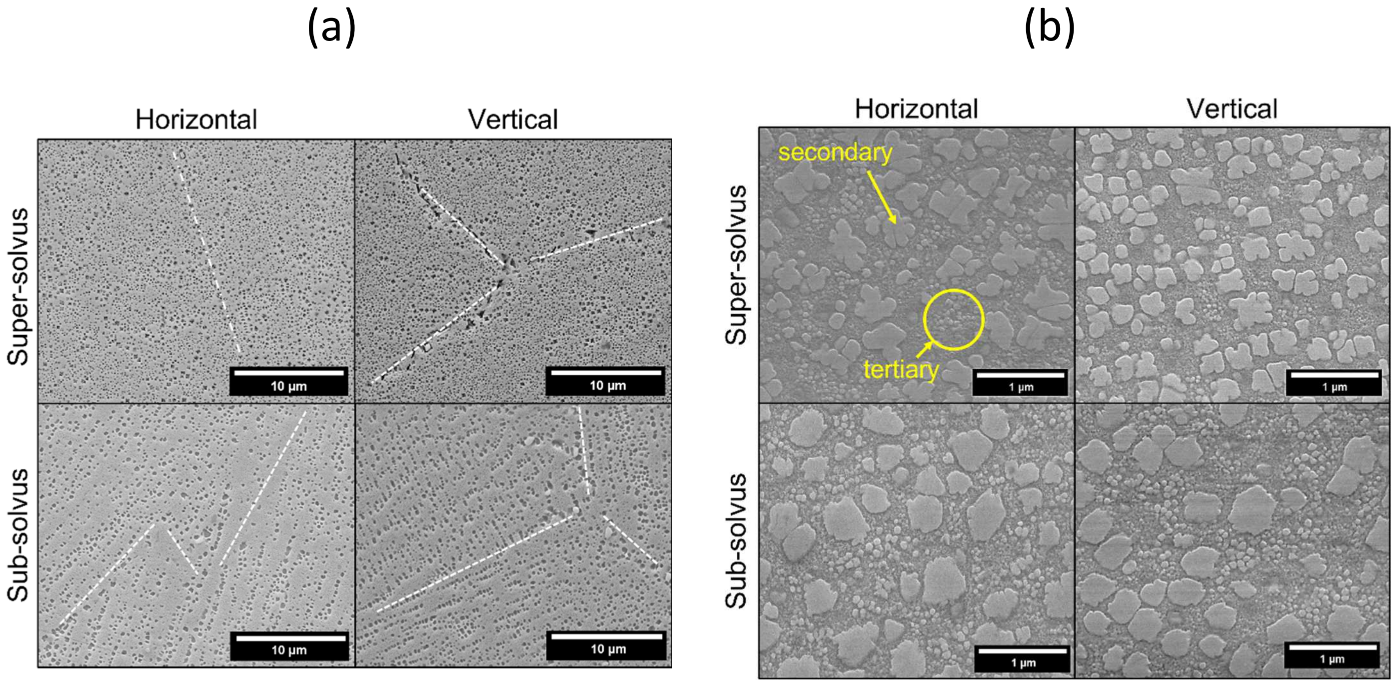

Figure 4: SEM micrographs of the as-received Rene 65 etched with: (a) aqua regia (backscattered electrons detection mode, dashed lines represent the grain boundaries) and (b) oxalic acid (in secondary electrons detection mode).

Table 2: Surface fraction and average diameter of γ'-precipitates with the corresponding standard error of as-received samples measured using image analysis in the aqua regia etched surfaces.

	Horizontal super		**Vertical super**		**Horizontal sub**		**Vertical sub**	
γ' fraction (area %)	31.0 ± 1.8		32.1 ± 2.4		22.9 ± 1.2		22.3 ± 1.0	
Average diameter (nm)	**secondary**	**tertiary**	**secondary**	**tertiary**	**secondary**	**tertiary**	**secondary**	**tertiary**
	290.1 ± 126.3	56.1 ± 15.0	233.0 ± 59.2	40.7 ± 11.2	361.5 ± 136.2	62.3 ± 17.9	356.3 ± 81.5	62.9 ± 14.2

3.2. High temperature oxidation of Rene 65

3.2.1. Oxidation kinetics

From the characterization of the as received samples, the additively manufactured Rene 65 exhibit different microstructural features depending on the building direction and the heat treatment applied after manufacturing. In order to study the influence of these features on the early stages of oxidation, the samples were oxidized in air and in Ar at 700, 800 and 900 °C for 48 hours. The specific mass gains are plotted against time in Figure 5a and 5b, for oxidation in air and Ar, respectively. Irrespective of the oxidizing gas used, increasing the temperature results in greater specific mass gain. At 700 and 800 °C, the differences between both materials and atmospheres are negligible when considering the low values of specific mass gain. However, when the temperature was increased to 900 °C, the samples showed significant mass uptake compared to the lower temperatures.

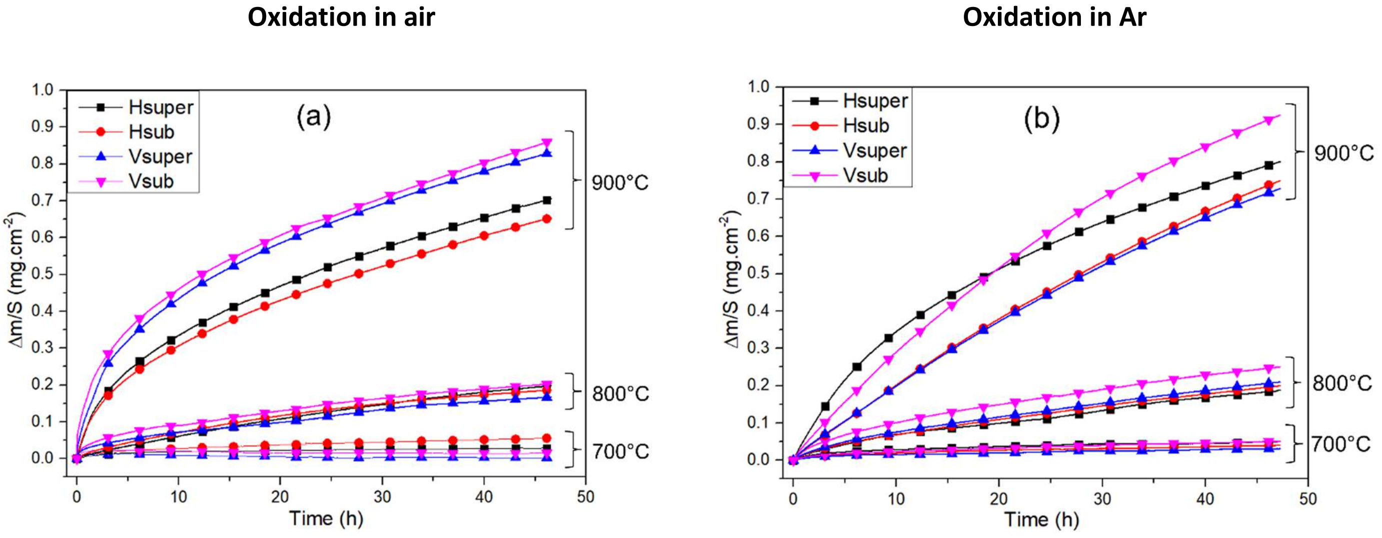
Oxidation in air

Oxidation in Ar

Figure 5: TGA evolution of specific mass gain against time (48h) for different oxidation temperatures (700, 800 and 900 °C) in (a) synthetic air (p_{O_2} = 0.2 bar) and (b) Ar (p_{O_2} = 2.10^{-6} bar).

In Figure 6, the linear fit of the specific mass gain against the square root of oxidation time shows that all the oxidation curves follow parabolic behavior with a R^2 between 0.976 and 0.998 irrespective of the temperature and the oxidizing gas. The parabolic rate constants k_p were determined by plotting the specific mass gains versus the square root of time using the equation (1) reported in Ref. [17], where C is a constant depending on the transient stage of oxidation. Parabolic rate constants were determined for each sample, except for Vertical super-solvus and sub-solvus because the specific mass gain was below the detection threshold of the scale after oxidation in air at 700 °C. The constants are gathered in Table 3.

$$\frac{\Delta m}{S} = \sqrt{k_p . t} + C \qquad (1)$$

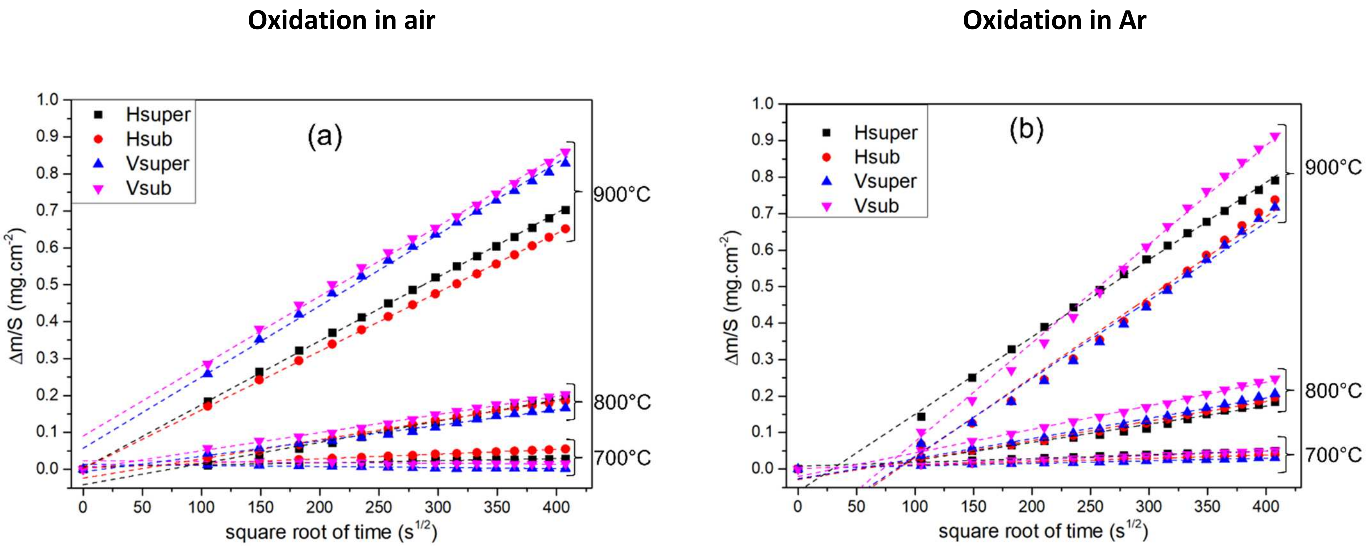
Oxidation in air

Oxidation in Ar

Figure 6: Linear fit of specific mass gain against the square root of time for different oxidation temperatures (700, 800 and 900 °C) in (a) synthetic air (p_{O_2} = 0.2 bar) and (b) Ar (p_{O_2} = 2.10^{-6} bar).

The parabolic rate constants are similar between all samples irrespective of the building direction, the heat treatment (super or sub-solvus) or the oxygen partial pressure (air or Ar). The Arrhenius plot representing the parabolic rate constants against the inverse of temperature of Figure 7 allows to calculate the activation energies (Ea) gathered in Table 3. All values of k_p are well above that of chromia formation in pure oxygen [18] and somewhat higher than those of the IN-718 and RR1000 disk superalloys but are close to those of similar alloys also employed for turbine disk applications like Udimet 720 (250 kJ.mol^{-1}), Astroloy (270 kJ.mol^{-1}) or Waspaloy (300 kJ.mol^{-1}) [14,19,20]. The activation energy corresponds to the formation of chromia on nickel-based superalloys [14,19,20].

Table 3: Parabolic rate constant k_p and activation energy for all samples after oxidation in air and argon at various temperatures for 48 hours.

	Temperature [°C]	Air			Argon		
		Mass gain [$mg.cm^{-2}$]	k_p [$g^2.cm^{-4}.s^{-1}$]	Ea [$kJ.mol^{-1}$]	Mass gain [$mg.cm^{-2}$]	k_p [$g^2.cm^{-4}.s^{-1}$]	Ea [$kJ.mol^{-1}$]
Horizontal super-solvus	700	0.028	$8.5\ 10^{-14}$	308	0.049	$3.3\ 10^{-13}$	271
	800	0.197	$1.5\ 10^{-11}$		0.185	$9.6\ 10^{-12}$	
	900	0.702	$1.1\ 10^{-10}$		0.793	$1.8\ 10^{-10}$	
Vertical super-solvus	700	0.002	-	260	0.031	$1.7\ 10^{-13}$	303
	800	0.166	$2.3\ 10^{-12}$		0.208	$3.1\ 10^{-12}$	
	900	0.828	$3.4\ 10^{-11}$		0.719	$5.1\ 10^{-11}$	
Horizontal sub-solvus	700	0.055	$5.9\ 10^{-13}$	235	0.039	$8.0\ 10^{-14}$	290
	800	0.186	$1.1\ 10^{-11}$		0.198	$3.6\ 10^{-12}$	
	900	0.652	$1.1\ 10^{-10}$		0.739	$5.4\ 10^{-11}$	
Vertical sub-solvus	700	0.015	-	291	0.050	$1.6\ 10^{-13}$	278
	800	0.202	$2.8\ 10^{-12}$		0.249	$4.5\ 10^{-12}$	
	900	0.859	$3.2\ 10^{-9}$		0.914	$7.1\ 10^{-11}$	
Cr_2O_3 [18]	700		$8.22\ 10^{-15}$	171			
	800		$6.95\ 10^{-14}$				
	900		$3.02\ 10^{-13}$				

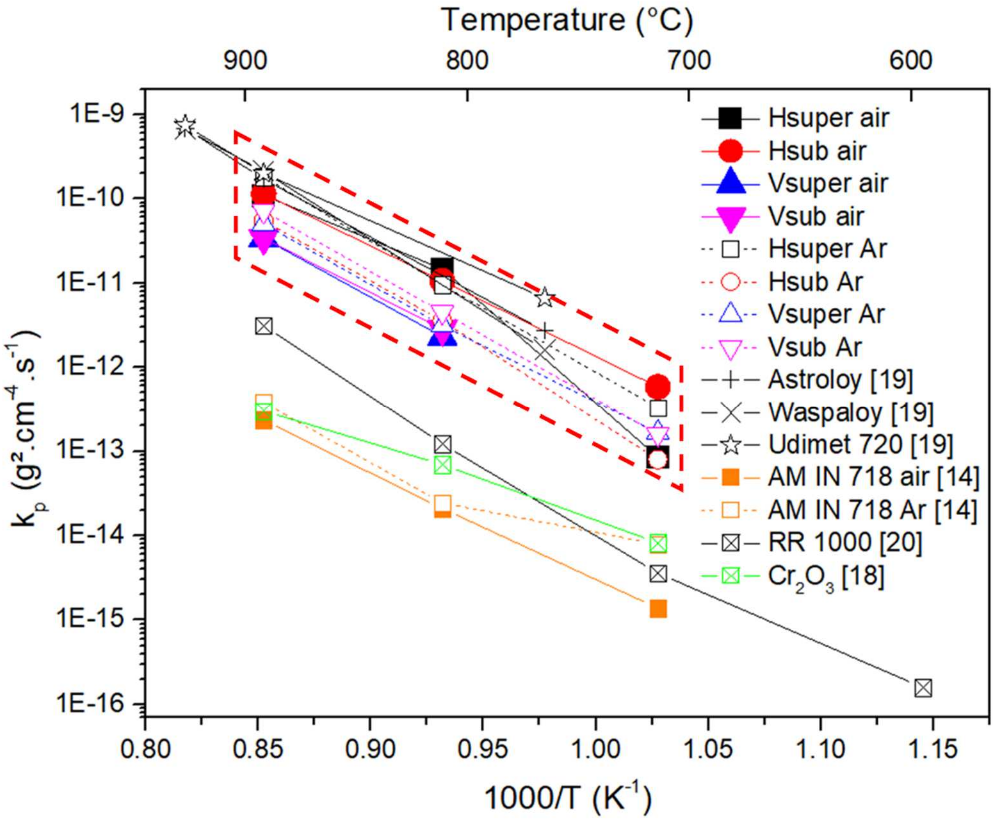

Figure 7: Arrhenius plot with the experimental data for the oxidation of AM Rene 65 in air (full symbols) and Ar (empty symbols) with data from the literature for the oxidation of pure chromium in purified oxygen [18], disk turbines alloys [19,20] and AM IN718 [14].

3.2.2. Surface characterization

The nature of the oxide layer was determined by combining the XRD, Raman and EDS analyses. Figure 8 shows the X-ray patterns of all four samples after oxidation in air and Ar. It is worth recalling that the signal of the oxides formed in the external scale was maximized due to the X-ray low incidence angle used. Therefore, the signals of the γ/γ′ (doublet) substrate peaks decrease with increasing oxidation temperature, in particular after 48 hours of exposure at 900 °C for which the oxide scale is assumed to be thicker. After oxidation in air (Figure 8a), the increase of temperature from 700 to 900 °C increases the contribution of Cr_2O_3 (ICDD 01-070-3765) and of rutile TiO_2 (ICDD 00-021-1276) whereas the response of spinel $NiCr_2O_4$ (ICDD 75-1728) remains similar.

In contrast, the oxide layer composition is slightly different in Ar than in air, especially at 900 °C as shown in Figure 8b. Indeed, the oxide layer formed in Ar is mainly composed of Cr_2O_3 as $NiCr_2O_4$ and the rutile TiO_2 peaks are less intense than after oxidation in air. Also, Ti seems to incorporate in a mixed (Cr,Ti) oxide (ICDD 01-082-0211, named “ct”) instead of the rutile TiO_2 detected in air. At the highest temperature of 900 °C, the oxide layer mainly consists of Cr_2O_3 on all samples, irrespective of the substrate and the oxygen partial pressure.

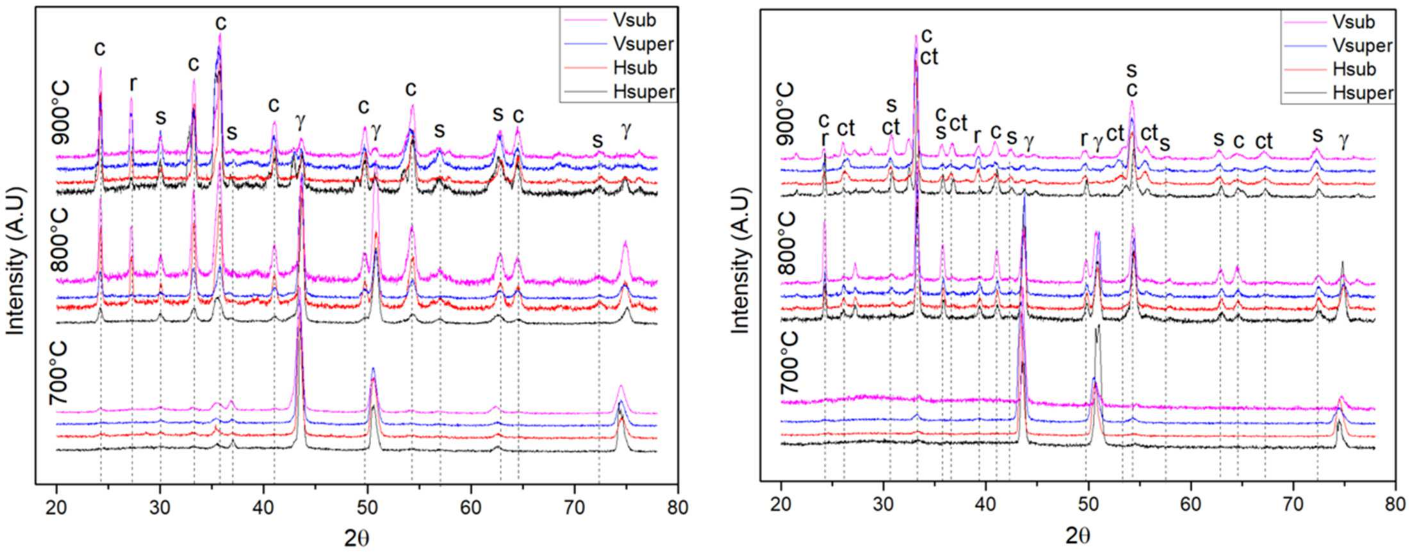

(a) air **(b) Ar**

γ: matrix, **c**: Cr_2O_3, **r**: rutile TiO_2, **ct**: $(Cr,Ti)_2O_3$, **s**: spinel $NiCr_2O_4$

Figure 8: Grazing incidence (5°) XRD patterns of all four samples after oxidation in air (a) and Ar (b) for 48h between 700 and 900 °C.

In addition to the difference in composition as a function of oxygen partial pressure, the oxide morphology differs between air and Ar. In order to compare both the effect of heat treatment and building direction on the oxide morphology, the two samples horizontal sub-solvus and vertical super-solvus are compared in Figure 9 and Figure 10 after oxidation in air and Ar, respectively. At 700 °C, irrespective of the oxygen partial pressure, the oxide layer is composed of small nodules rich in nickel and chromium that have been identified as Cr_2O_3 and $NiCr_2O_4$ by XRD and Raman micro-spectrometry analyses. After oxidation in air, the oxide layer is composed of equiaxed grains whose size increases with temperature. The amount of chromium increases compared to the oxide layer at 700 °C. However, after oxidation in Ar in Figure 10, the oxide layer is composed of ridges with a higher amount of titanium. The morphology of the oxide layer does not seem to be influenced by the metallurgical differences of the substrates but mostly by the type of annealing gas.

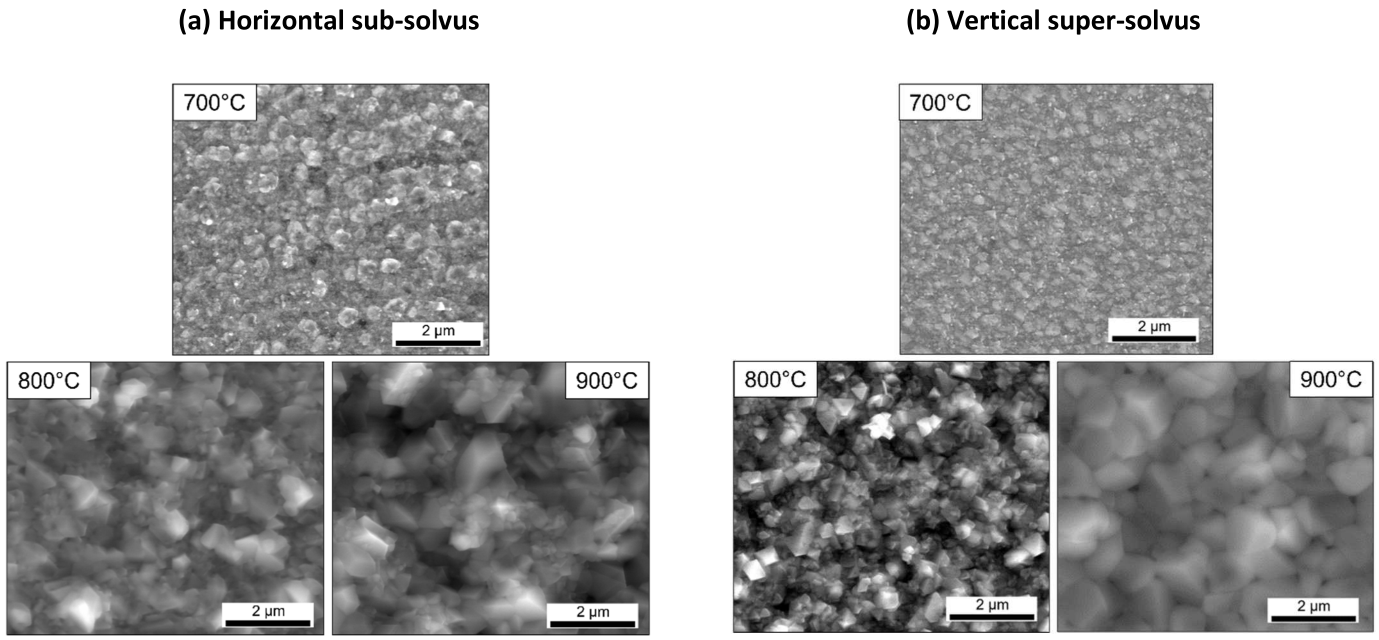

Figure 9: SEM (secondary electrons) micrographs of the oxide morphologies of Rene 65 (a) horizontal sub-solvus and (b) vertical super-solvus samples after 48 hours of oxidation in synthetic air

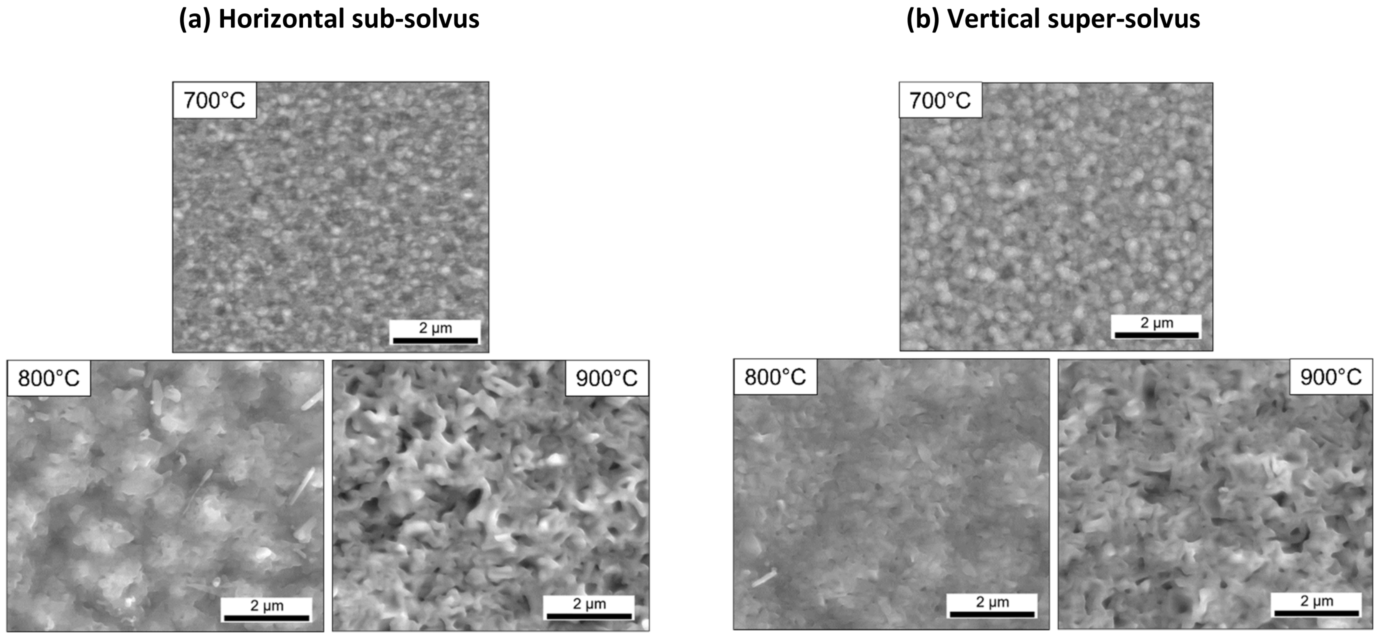

Figure 10: SEM (secondary electrons) micrographs of the oxide morphologies of Rene 65 (a) horizontal sub-solvus and (b) vertical super-solvus samples after 48 hours of oxidation in Ar.

3.2.3. Cross section characterization

To understand how the oxidizing gas affects the oxide growth, the cross sections were prepared and analyzed by SEM with high magnification and displayed in Figure 11 and Figure 12 after oxidation in air and Ar, respectively. Only the horizontal sub-solvus and vertical super-solvus are displayed since they exemplify all samples.

At 700 °C, the oxide layer is about 250 nm thick irrespective of the substrate and the oxidizing gas and is composed of nickel, chromium and oxygen as confirmed by EDS analyses. At 800 °C, the oxide layer is about 1 µm thick and composed of a chromia layer above a thin alumina scale. The diffusion of aluminum to form the underlying scale led to the formation of a γ'-Ni_3(Al,Ti) depleted area of about 2 µm thick below the oxide scale. It is also noticeable that the penetration of oxygen along the grain boundaries results in alumina decorations (marked in red dotted lines). At 900 °C in air, the chromia layer is about 3 µm thick and the γ'-Ni_3(Al,Ti) depleted area is about 10 µm thick with many titanium nitrides as confirmed by EDS X-rays maps in Figure 13a. The alumina decorations are also deeper, especially at grain boundaries.

After oxidation in Ar (Figure 12), the multilayered character is similar to the one observed after oxidation in air with the same chromia thickness of about 1 µm at 800 °C above a 2 µm deep γ'-Ni_3(Al,Ti) depleted area. In contrast, Figure 13b shows that the external oxide is significantly rich in Ti (> 10 at.%) resulting in the depletion of Ti (< 2 at.%) in the y'-Ni_3(Al,Ti) when Rene 65 is oxidized at 900 °C under Ar. The morphology of the alumina penetrations is also different and is much finer and deeper than those obtained under air.

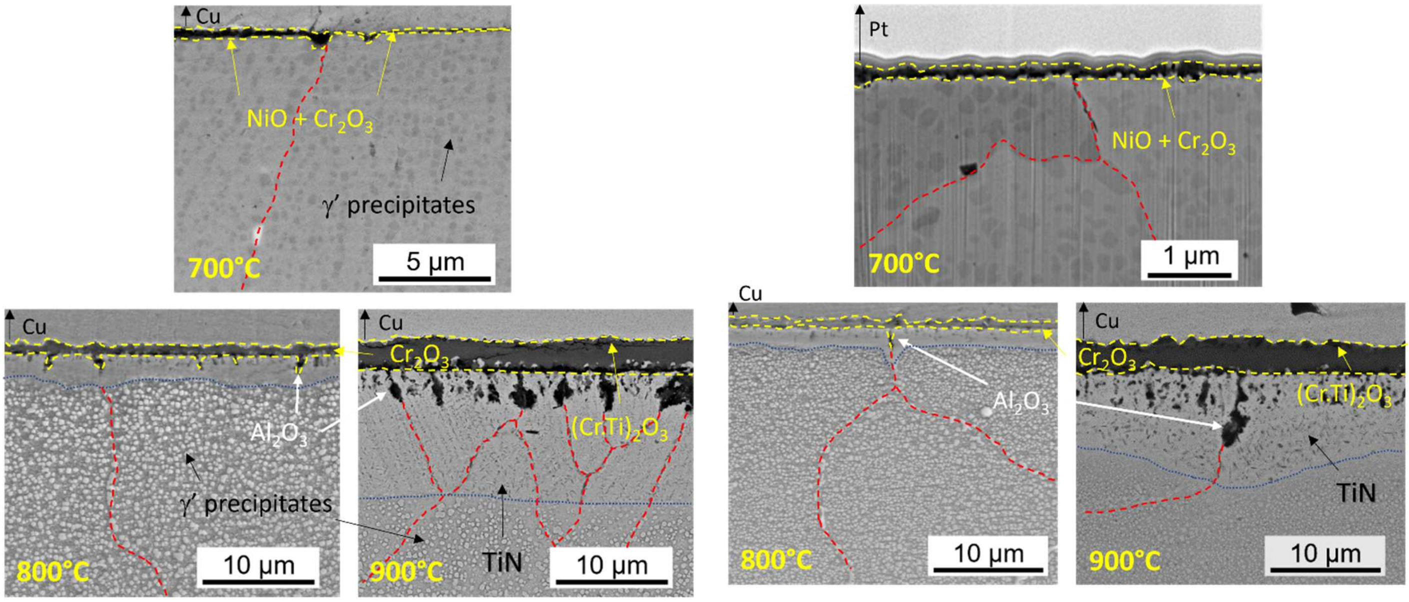
(a) Horizontal sub-solvus

(b) Vertical super-solvus

Figure 11: SEM (secondary electrons) micrographs of the cross sections of Rene 65 (a) horizontal sub-solvus and (b)

vertical super-solvus samples after 48 hours of oxidation in synthetic air.

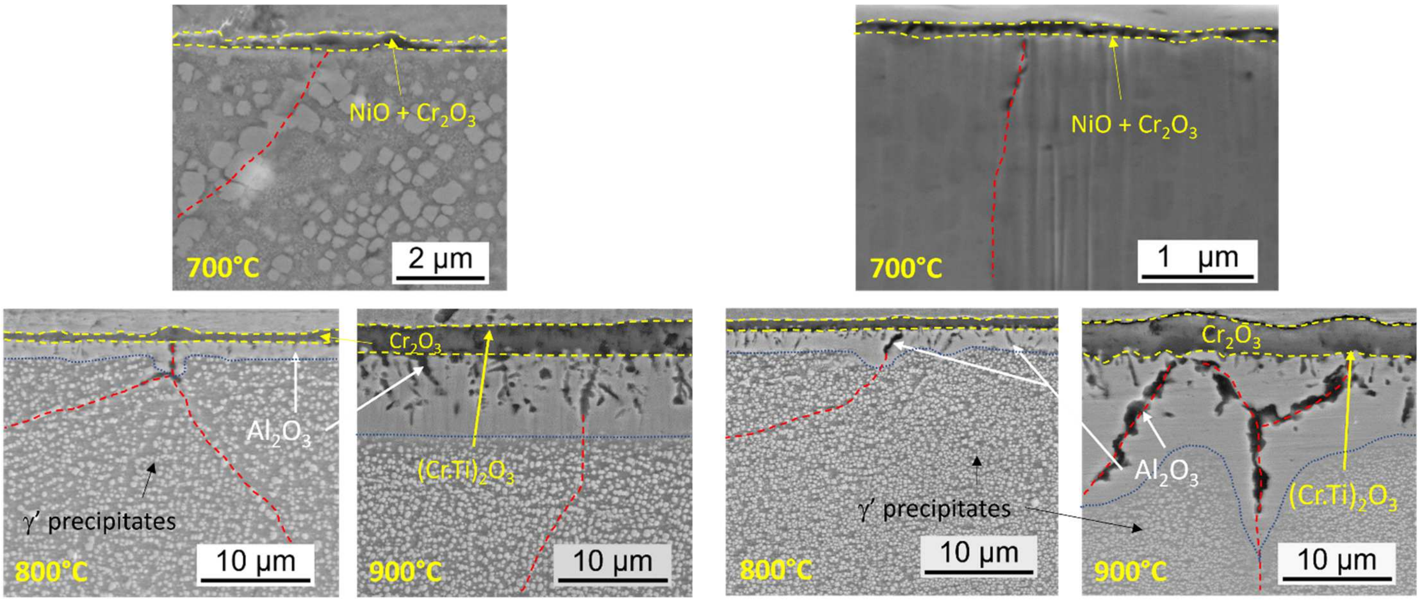
(a) Horizontal sub-solvus

(b) Vertical super-solvus

Figure 12: SEM (secondary electrons) micrography of the cross sections of Rene 65 (a) horizontal sub-solvus and (b) vertical super-solvus samples after 48 hours of oxidation in Ar.

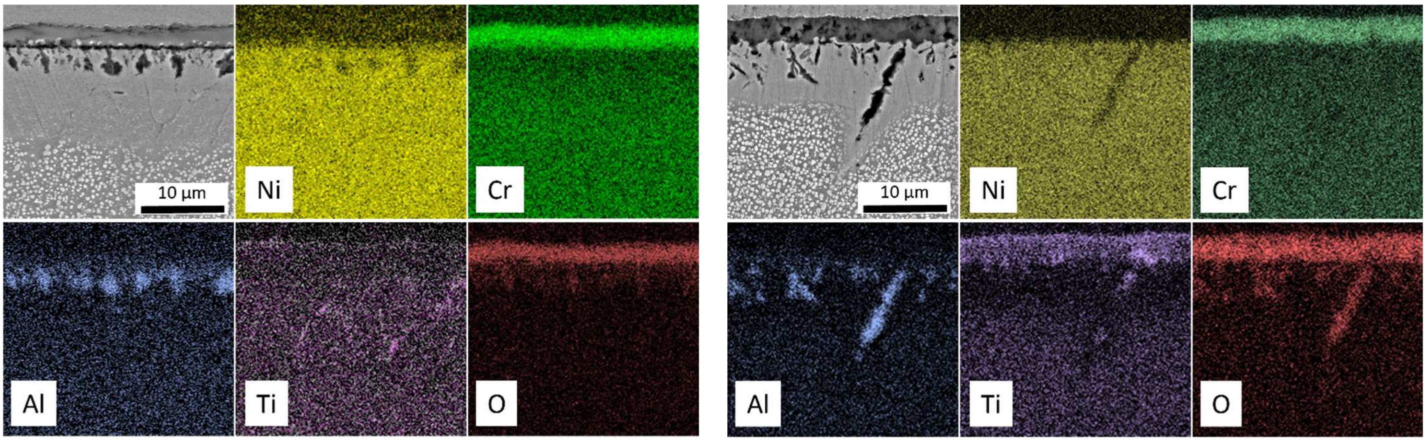
(a) Horizontal sub-solvus in air at 900 °C

(b) Horizontal sub-solvus in Ar at 900 °C

Figure 13: EDS mapping on cross sections of Horizontal sub-solvus sample oxidized at 900 °C in (a) air and (b) Ar for 48 hours.

4. Discussion

4.1. As received material

The chemical composition of AM Rene 65 was given in Table 1. Although EDS may not be the most accurate technique to precisely determine the composition of samples, in particular that of light elements or those in too small quantities, the results show that all four Rene 65 samples are chemically very similar.

From the 3D models (Figure 2), it has been shown that the microstructure of AM Rene 65 is highly dependent on the building direction and on the heat treatment. Such microstructures are equivalent to those reported by Wessman et al. for the same material and process [7]. As reported in various articles, the microstructure observed in sub-solvus samples, with elongated grains oriented in the direction parallel to the building direction, is typical of materials made by additive manufacturing [21,22]. This solidification structure is dependent on both crystallographic orientation of the previous layer and local heat flow direction. Indeed, during solidification of the melted layer, competitive growth occurs among dendrites with various crystallographic orientations. Columnar structures develop when the dendrites mostly aligned with the temperature gradient outgrow the slower growing misaligned dendrites [21–24]. On the one hand, the sub-solvus heat treatment retains part of the dendritic structure, which results in these columnar grains that are oriented in the [100] direction as shown by EBSD analysis of Figure 3. On the other hand, the super-solvus heat treatment completely removes the dendritic microstructure and allows grain growth leading to an equiaxed microstructure (i.e. non-textured) independently of the initial manufacturing direction.

The microstructure of the AM Rene 65 is different from that of wrought Rene 65 which has been studied in the sub-solvus and super-solvus form by other authors [2,4,13]. The sub-solvus heat treated Rene 65 retains about 10-15% of primary γ', resulting in a fine grain microstructure as the primary γ' precipitates pin the grains boundaries (Zener pinning effect) [25]. In contrast, the grain size of the super-solvus microstructure observed by Bond et al. on forged ingot was about 1 mm average which is ~15 times larger than the one observed for the AM Rene 65, because the dissolved precipitates can no longer prevent grain growth [4,10,13].

Forged Rene 65 contains three population of γ' precipitates, primary, secondary, and tertiary, depending on their nucleation temperature. The formation process of theses precipitates has been explained by Singh et al. on Rene 88DT [26]. According to Laurence et al. study, primary precipitates represent about 10 vol.% and secondary and tertiary precipitates represent around 20 vol.% on the sub-solvus forged Rene 65 [27]. AM Rene 65 also present around 20% of secondary and tertiary precipitates after sub-solvus heat treatment as shown in Figure 4 and Table 2, however the area % of γ' precipitates is higher after super-solvus heat treatment. However, in none of the cases primary precipitates were observed. During the AM process, the high thermal gradients and the cooling rates generated do not allow the formation of primary precipitates. Only secondary and tertiary γ' precipitates were found, and the differences observed between super-solvus and sub-solvus are mainly due to the heat treatment applied after the DMLM building process that impact the size and shape of the precipitates as studied by Wessman et al. and Katsari et al. [10,12].

In the study on the mechanical properties of AM Rene 65, Wessman et al. showed that most of the crack initiation sites in low cycle fatigue at 650 °C were located at the surface of the samples, suggesting an impact of the surface condition on the crack initiation process [7]. A similar observation was done by A. Laurence in her PhD thesis work using C&W Rene 65 material tested in low cycle fatigue (LCF) at 700 °C [13], or by Govaere et al. using C&W AD730 (a very similar alloy to Rene 65) tested in the same LCF conditions [28] showing that in both cases, fatigue crack initiation is controlled by oxidation of primary γ' precipitates. The study of oxidation mechanisms is therefore particularly important for turbine disk materials.

4.2. Influence of the oxygen partial pressure on the oxidation behavior

As shown in the TGA analyses of Figure 5, the specific mass gain of AM Rene 65 in air becomes significant from 700 °C. Despite the metallurgical differences between the four different samples, the oxidation behavior of AM Rene 65 was studied and using the parabolic approximation, the parabolic rate constants in synthetic air and in Ar were then determined by TGA and compared with that of AM IN718, powder metallurgy forged RR1000 alloys and turbine disks alloys [14,19,20] and gathered in Figure 7. The values of $\log(k_p)$ for the samples of AM Rene 65 are higher than those calculated by Juillet et al. for an AM IN718 alloy, but similar to those of Chen et al. for alloys with Cr and Co contents similar to those of Rene 65 [14,19]. However, the activation energies of AM Rene 65 are higher than those obtained by Juillet on AM IN718 (200 $kJ.mol^{-1}$ in air and 151 $kJ.mol^{-1}$ in argon) [14]. These differences could be explained by the growth of a much denser Cr_2O_3 oxide scale like England and Virkar showed under isothermal condition in air on IN718 [29].

Additionally, a similar alloy was studied by Romain et al. in the same temperature range but for longer times, with a composition close to the one of Rene 65, at the exception of the Mo and W content [30]. Romain et al. calculated the same activation energy (314 $kJ.mol^{-1}$) than the AM Rene 65 of this study and observed TiO_2 after exposure in air at 800 °C but also NiO at 900 °C after 100 hours of exposure. As a matter of fact, Cr_2O_3 is known to be effective to protect against oxidation till ~870 °C as it could become unstable and volatile above this critical temperature. Therefore, longer annealing at 900 °C could probably lead to the formation of other oxides such as NiO. Secondly, the (supposed) absence of Mo and W in the alloy used by Romain et al. could be critical at high temperatures as some reports indicates that these elements could help stabilizing the Cr_2O_3 layer due to the high valence of Mo and W that reduce metal vacancy in the Cr_2O_3 layer [31].

The oxidation results of AM Rene 65 show that the metallurgical differences between the samples do not significantly affect the oxidation behavior from a kinetics point of view. Moreover, neither the microstructure nor the γ' precipitates are affected by temperature after 48 hours of exposures which is consistent with the literature that states that Rene 65 can be used for temperature up to 760 °C for more than 100 hours without any noticeable microstructural change [10]. However, the characterization of the oxide layer by XRD (Figure 8) and by SEM-EDS (Figure 9 to Figure 13) shows that the AM Rene 65 behaves differently depending on the oxygen partial pressure. At 48h at 700 °C (Figure 14a), the oxide layers are similar with the formation of a spinel $NiCr_2O_4$ resulting from the combined oxidation of nickel (NiO) and chromium (Cr_2O_3) [32]. However, the oxidation of chromium is favored over the oxidation of nickel leading to the dissolution of NiO nodules and the formation of the spinel due to the reduced oxygen partial pressure [33].

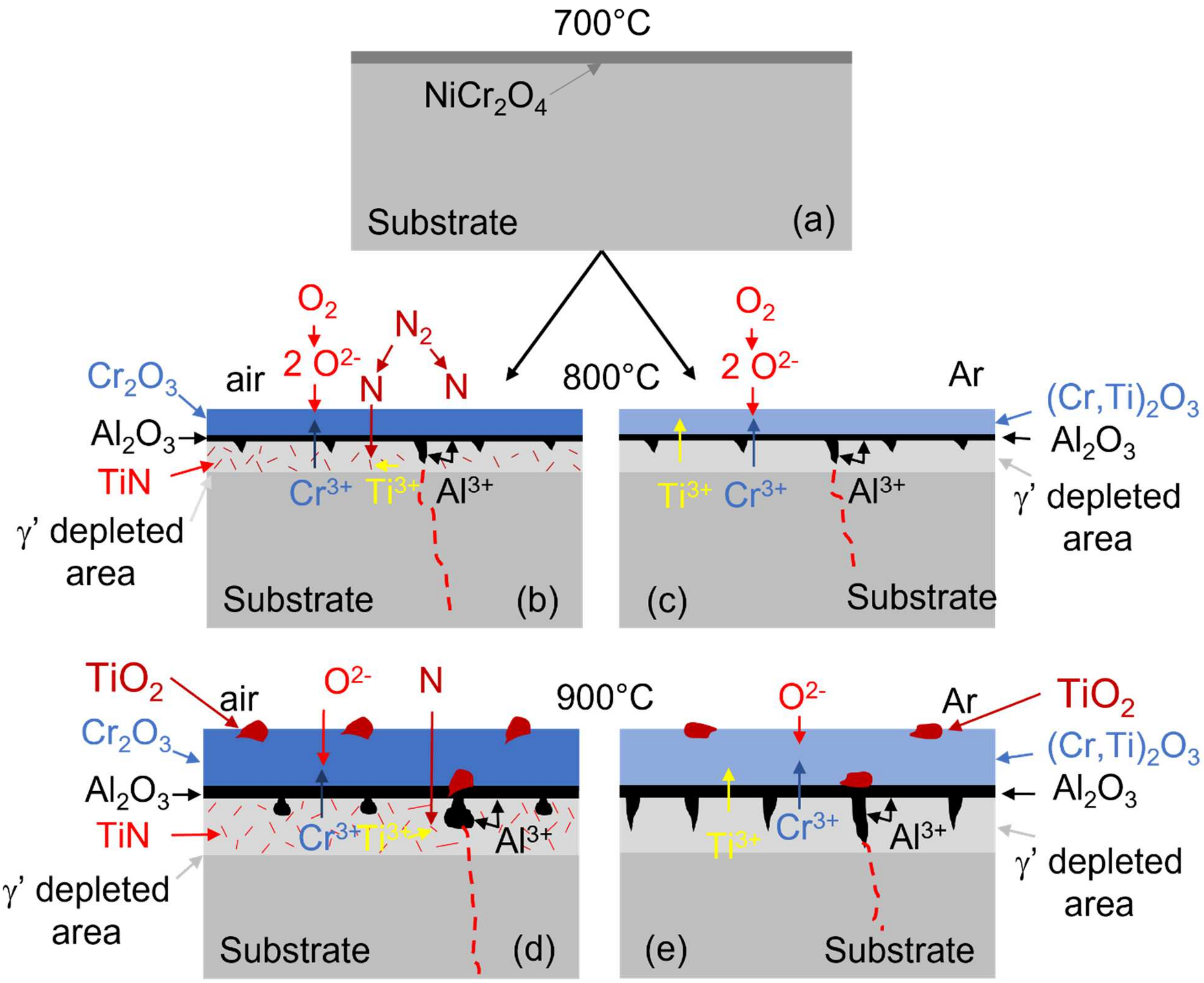

Figure 14: Schematic diagram illustrating the oxidation mechanisms for Rene 65 AM depending on the temperature and oxygen partial pressure after 48 hours.

The differences related to the oxidizing gas appear from 800 °C with the formation of titanium nitrides after oxidation in air (Figure 14b) due to the diffusion of nitrogen through the external chromia and internal alumina layers [34]. Since there is no nitrogen in the Ar gas (Figure 14c), the titanium nitrides do not form. Therefore, titanium is free to diffuse and leads to a Ti-doped Cr_2O_3 scale that creates vacancies and fosters further oxidation [20]. The outward diffusion of Cr^{3+} and of Ti^{4+} ions as dopants of chromia was also reported by Cruchley et al. upon the oxidation of RR1000 alloy in air [20]. In addition, the diffusion of Ti and Al towards the substrate/oxide interface leads to a γ′ depleted zone underneath the oxide layer. The local decrease in Al and Ti content below the surface leads to the dissolution of the γ′-phase which is no longer stabilized. Simultaneously, the unbalanced flow of cations and anions brings about the formation of vacancies and pores (Kirkendall porosity) at the oxide/substrate interface, as e.g., Pedraza et al. showed for the oxidation of AM1 Ni-based superalloy [33]. At 900 °C, all these phenomena are exacerbated and lead to the formation of a thicker oxide layer with a deeper γ' depleted layer than at 800 °C for the same oxidation time.

In addition to the outward formation of chromia, AM Rene 65 undergoes preferential grain boundary oxidation (Figure 11 and Figure 12). The grain boundaries also have a role to play in the oxidation as they gather aluminum and titanium that have high affinity with oxygen and are thus sensitive to oxidation at low partial pressure of oxygen p_{O_2} below the chromia layer [35]. The results obtained are in agreement with the intergranular oxidation model proposed by Sanviemvongsak et al. on AM IN718 which states that intergranular oxidation is controlled by both the diffusion of oxygen at the oxide/metal interface and the slower diffusion of Al and Ti towards the grain boundaries [35].

5. Conclusions

The characterization of DMLM fabricated Rene 65 with two building directions (vertical and horizontal) and heat treatments (super and sub-solvus) demonstrated that the latter affect the final microstructure as the sub-solvus samples retain the orientation of the building direction whereas the super-solvus heat treatment deletes it. However, the different microstructures generated by both building direction and heat treatment do not markedly affect the oxidation kinetics after 48 hours of exposure whereas the oxidizing gas changes the oxidation mechanisms. At 700 °C, the oxide scale is composed of spinel $NiCr_2O_4$ and Cr_2O_3. After oxidation in synthetic air, the oxide layer is composed of a chromia layer at the gas/oxide interface and an alumina layer at the oxide/metal interface. The diffusion of aluminum leads to a depletion of γ' precipitates in the sub-surface while the diffusion of nitrogen through the oxide layer allows the formation of titanium nitrides in the depleted area. On the contrary, after oxidation in Ar, the absence of nitrogen allows the free diffusion of titanium leading to a chromia doped oxide layer at the gas/oxide interface on top of an alumina layer at the oxide/metal interface. In both atmospheres, the increase of temperature leads to the increase of the oxide thickness, deeper depleted area, and further internal oxidation at grain boundaries due to diffusion of titanium and aluminium during oxidation. Furthermore, the calculation of the oxidation kinetics showed that the oxidation behavior of AM Rene 65 is similar to that of other γ'-strengthened disk alloys with similar compositions according to the activation energy calculated from an Arrhenius plot.

Data availability

The raw/processed data required to reproduce these findings are available upon request from the corresponding authors.

Acknowledgements

The authors are grateful to GE Additive and, more specifically, to Dr. Andrew Wessman (formerly at GE Additive and now at the University of Arizona in Tucson) for providing almost defect-free AM processed Rene 65 specimens.

6. References

[1] M. C. Hardy, M. Detrois, E. T. Mcdevitt, C. Argyrakis, V. Saraf, P. D. Jablonsky, J. A. Hawk, R. C. Buckingham, H. S. Kitaguchi and S. Tin, « Solving Recent Challenges for Wrought Ni-Base Superalloys », *Metall. Mater. Trans. A*, Vol. 51, 2020, doi: 10.1007/s11661-020-05773-6.

[2] J. A. Heaney, M. L. Lasonde, A. M. Powell, B. J. Bond, and C. O'Brien, « Development of a new cast and wrought alloy (Rene 65) for high temperature disk applications », *8th Int. Symp. Superalloy 718 Deriv.*, 2014, doi: 10.1002/9781119016854.ch6.

[3] R. L. Kennedy, « Allvac 718Plus, Superalloy for the Next Forty Years », in *Superalloys 718, 625, 706 and Various Derivatives (2005)*, TMS, 2005, doi: 10.7449/2005/Superalloys_2005_1_14.

[4] B. J. Bond, C. O'Brien, J. L. Russell, J. A. Heaney, and M. L. Lasonde, « René 65 Billet Material for Forged Turbine Components », *8th Int. Symp. Superalloy 718 Deriv.*, 2014, doi: 10.1002/9781119016854.ch9.

[5] W. Gao, Y. Zhang, D. Ramanujan, K. Ramani, Y. Chen, C. B. Williams, C. L. Wang, Y. C. Shin, S. Zang and P. D. Zavattieri, « The status, challenges, and future of additive manufacturing in engineering », *Comput.-Aided Des.*, Vol. 69, 2015, doi: 10.1016/j.cad.2015.04.001..

[6] T. Pereira, J. V. Kennedy, and J. Potgieter, « A comparison of traditional manufacturing vs additive manufacturing, the best method for the job », *Procedia Manuf.*, Vol. 30, 2019, doi: 10.1016/j.promfg.2019.02.003.

[7] A. Wessman, J. Cormier, F. Hamon, K. Rainey, S. Tin, D. Tiparti and L. Dial, « Microstructure and mechanical properties of additively manufactured Rene 65 », *Superalloys 2020*, 2020, doi: 10.1007/978-3-030-51834-9_94

[8] J. J. Lewandowski and M. Seifi, « Metal Additive Manufacturing: A Review of Mechanical Properties », Annu. Rev. Mater. Res., Vol. 46, 2016, doi: 10.1146/annurev-matsci-070115-032024.

[9] M. Seifi, A. Salem, J. Beuth, O. Harrysson, and J. J. Lewandowski, « Overview of Materials Qualification Needs for Metal Additive Manufacturing », JOM, Vol. 68, 2016, doi: 10.1007/s11837-015-1810-0.

[10] A. Wessman, A. Laurence, J. Cormier, P. Villechaise, T. Billot, and J.-M. Franchet, « Thermal Stability of Cast and Wrought Alloy Rene 65 », Superalloys 2016 Proc. Of the 13th Int. Symp. Superalloys, 2016, doi: 10.7449/Superalloys/2016/Superalloys_2016_793_800.

[11] C. M. Katsari, H. Che, D. Guye, A. Wessman, and S. Yue, « Microstructural Characterization and Mechanical Properties of Rene 65 Precipitates », Proc. 9th Int. Symp. Superalloy 718 Deriv., 2018, doi: 10.1007/978-3-319-89480-5_41.

[12] C.-M. Katsari, S. Katnagallu, and S. Yue, « Microstructural characterization of three different size of gamma prime precipitates in Rene 65 », Mater. Charact., Vol. 169, nov. 2020, doi: 10.1016/j.matchar.2020.110542.

[13] A. Laurence, J. Cormier, P. Villechaise, T. Billot, J-M. Franchet, F. Pettinari-Sturmel, M. Hantcherli, F. Mompiou and A. Wessman « Impact of the Solution Cooling Rate and of Thermal Aging on the Creep Properties of the New Cast & Wrought René 65 Ni-Based Superalloy », 8th Int. Symp. Superalloy 718 Deriv., 2014, doi: 10.1002/9781119016854.ch27.

[14] C. Juillet, A. Oudriss, J. Balmain, X. Feaugas, and F. Pedraza, « Characterization and oxidation resistance of additive manufactured and forged IN718 Ni-based superalloys », Corros. Sci., Vol. 142, 2018, doi: 10.1016/j.corsci.2018.07.032.

[15] L. Bataillou, L. Martinelli, C. Desgranges, S. Bosonnet, K. Ginestar, et al., « Growth Kinetics and Characterization of Chromia Scales Formed on Ni–30Cr Alloy in Impure Argon at 700 °C », Oxid. Met., Vol. 93, 2020, doi: 10.1007/s11085-020-09958-7.

[16] R. Salehi, A. Samadi, and M. Kh. Savadkoohi, « Influence of Etchants on Quantitative/Qualitative Evaluations of the γ′ Precipitates in a Nickel-Base Superalloy », *Metallogr. Microstruct. Anal.*, Vol. 1, 2012, doi: 10.1007/s13632-012-0043-7.

[17] B. Pieraggi, « Calculations of parabolic reaction rate constants », *Oxid. Met.*, Vol. 27, 1987, doi: 10.1007/BF00667057.

[18] E. A. Gulbransen and K. F. Andrew, « Kinetics of the Oxidation of Chromium », *J. Electrochem. Soc.*, Vol. 104, 1957, doi: 10.1149/1.2428576.

[19] J. H. Chen, P. M. Rogers, and J. A. Little, « Oxidation behavior of several chromia-forming commercial nickel-base superalloys », *Oxid. Met.*, Vol. 47, 1997, doi: 10.1007/BF02134783.

[20] S. Cruchley, H. E. Evans, M. P. Taylor, M. C. Hardy, and S. Stekovic, « Chromia layer growth on a Ni-based superalloy: Sub-parabolic kinetics and the role of titanium », *Corros. Sci.*, Vol. 75, 2013, doi: 10.1016/j.corsci.2013.05.016.

[21] N. K. Adomako, N. Haghdadi, and S. Primig, « Electron and laser-based additive manufacturing of Ni-based superalloys: A review of heterogeneities in microstructure and mechanical properties », *Mater. Des.*, Vol. 223, 2022, doi: 10.1016/j.matdes.2022.111245.

[22] A. Basak and S. Das, « Epitaxy and Microstructure Evolution in Metal Additive Manufacturing », *Annu. Rev. Mater. Res.*, Vol. 46, 2016, doi: 10.1146/annurev-matsci-070115-031728.

[23] T. DebRoy, H. L. Wei, J. S. Zuback, T. Mukherjee, J. W. Elmer, J. O. Milewski, A. M. Beese, A. Wilson-Heid, A. De and W. Zhank, « Additive manufacturing of metallic components – Process, structure and properties », *Prog. Mater. Sci.*, Vol. 92, 2018, doi: 10.1016/j.pmatsci.2017.10.001.

[24] T. Trosch, J. Strößner, R. Völkl, and U. Glatzel, « Microstructure and mechanical properties of selective laser melted Inconel 718 compared to forging and casting », *Mater. Lett.*, Vol. 162, 2016, doi: 10.1016/j.matlet.2015.10.136.

[25] K. Song and M. Aindow, « Grain growth and particle pinning in a model Ni-based superalloy », *Mater. Sci. Eng. A*, Vol. 479, 2008, doi: 10.1016/j.msea.2007.09.055.

[26] A.R.P. Singh, S. Nag, S. Chattopadhyay, Y. Ren, J. Tiley, G.B. Viswanathan, H.L. Fraser, R. Banerjee, « Mechanisms related to different generations of γ′ precipitation during continuous cooling of a nickel base superalloy », *Acta Mater.*, Vol. 61, 2013, doi: 10.1016/j.actamat.2012.09.058.

[27] A. Laurence, « Impact du sur-vieillissement métallurgique sur le comportement et la durabilité du nouveau superalliage pour disque de turbine René 65 », PhD thesis, ISAE-ENSMA, 2016.

[28] A. Govaere, A-L. Rouffié, J-M. Franchet, J. Galy, C. Dumont, A. Devaux, C. Crozet, and J. Cormier « Is the Carbon Content Really an Issue for the LCF Durability of Forged γ/γ′ Ni-Based Disk Alloys? », *8th Int. Symp. Superalloy 718 Deriv.*, 2020, doi: 10.1007/978-3-030-51834-9_57

[29] D. M. England and A. V. Virkar, « Oxidation Kinetics of Some Nickel-Based Superalloy Foils and Electronic Resistance of the Oxide Scale Formed in Air Part I », *J. Electrochem. Soc.*, Vol. 146, 1999, doi: 10.1149/1.1392454.

[30] C. Romain, D. Texier, C. Desgranges, J. Cormier, S. Knittel, D. Monceau and D. Delagnes « Oxidation of Thin Nickel-Based Superalloy Specimens: Kinetics Study and Mechanical Integrity », *Oxid. Met.*, Vol. 96, 2021, doi: 10.1007/s11085-021-10075-2.

[31] S.-J. Park, S.-M. Seo, Y.-S. Yoo, H.-W. Jeong, and H. Jang, « Effects of Cr, W, and Mo on the High Temperature Oxidation of Ni-Based Superalloys », *Materials*, Vol. 12, 2019, doi: 10.3390/ma12182934.

[32] D.-S. Li, G. Chen, D. Li, Q. Zheng, P. Gao, and L.-L. Zhang, « Oxidation resistance of nickel-based superalloy Inconel 600 in air at different temperatures », *Rare Met.*, Vol. 40, 2021, doi: 10.1007/s12598-018-1148-1.

[33] F. Pedraza, R. Troncy, A. Pasquet, J. Delautre, and S. Hamadi, « Critical Hafnium Content for Extended Lifetime of AM1 Single Crystal Superalloy », *Superalloys 2020*, 2020, doi: 10.1007/978-3-030-51834-9_76.

[34] U. Krupp and H.-J. Christ, « Selective oxidation and internal nitridation during high-temperature exposure of single-crystalline nickel-base superalloys », *Metall. Mater. Trans. A*, Vol. 31, n° 1, 2000, doi: 10.1007/s11661-000-0051-0.

[35] T. Sanviemvongsak, D. Monceau, C. Desgranges, and B. Macquaire, « Intergranular oxidation of Ni-base alloy 718 with a focus on additive manufacturing », *Corros. Sci.*, Vol. 170, 2020, doi: 10.1016/j.corsci.2020.108684.